

# Hard/Soft NLoS Detection via Combinatorial Data Augmentation for 6G Positioning

Sang-Hyeok Kim, Seung Min Yu, Jihong Park, *Senior Member, IEEE*, and Seung-Woo Ko, *Senior Member, IEEE*

**Abstract**—A key enabler for achieving the stringent requirements of 6G positioning is the ability to exploit site-dependent information that governs *line-of-sight* (LoS) and *Non-LoS* (NLoS) propagation. However, acquiring such environmental information in real-time remains challenging in practice. To address this issue, we propose a novel NLoS detection algorithm termed *combinatorial data augmentation-guided NLoS detection* (CDA-ND), which builds upon our prior work. CDA-ND generates numerous *preliminary estimated locations* (PELs) by applying multilateration over many different *gNodeB* (gNB) combinations using a single snapshot of range measurements. When a target gNB is in NLoS, the resulting PELs naturally split into two clusters: one derived using the target gNB’s range measurement, and the other derived without it. The displacement between the two clusters is represented by a single vector, called the *NLoS evidence vector* (NEV), which serves as a key feature for computing an NLoS likelihood score. Based on this score, two modes of NLoS detection are developed. First, each gNB is classified as LoS or NLoS, termed *hard decision* (HD), which can be designed on-the-fly via a simple threshold test on the NLoS likelihood score. Second, each gNB’s NLoS confidence is probabilistically quantified, termed *soft decision* (SD), which extends HD with weak site-survey priors, namely empirical NLoS-score samples and the average NLoS probability. We then design the subsequent positioning algorithms tailored to these two modes by excluding gNBs deemed NLoS (for both HD and SD) and re-weighting the remaining gNBs (for SD). The proposed CDA-ND achieves high reliability in indoor factory environments under frequency range 1, attaining NLoS detection accuracies of 96.6% and 91.1% when the proportion of NLoS gNBs is approximately 18% and 56%, respectively. As a result, a positioning algorithm integrating CDA-ND significantly improves positioning accuracy, achieving reductions of 20.04% and 65.99% in mean absolute error under LoS- and NLoS-dominant environments, respectively.

**Index Terms**—6G positioning, NLoS detection, NLoS evidence vector, combinatorial data augmentation, 3GPP indoor factory, hard/soft decision.

## I. INTRODUCTION

Positioning is expected to become a core capability of 6G networks, supporting the broader vision of tightly integrating sensing with communications [2]. Unlike current 5G positioning services, which largely localize a generic *user equipment* (UE) at roughly cell-coverage granularity, 6G positioning is envisioned to be context-specific, adapting to the

physical site and its temporal variations (e.g., smart factory and indoor office). Such context-aware designs can exploit environment-dependent characteristics to meet stringent 6G accuracy requirements for positioning and downstream tasks, as exemplified by *non-line-of-sight* (NLoS)-aware design using blockage-related cues (e.g., [3], [4]). However, obtaining and maintaining such context information in practice is challenging, calling for techniques that infer and leverage it directly from the current measurements without relying on prior knowledge. To address this challenge, this work builds upon our prior work on *combinatorial data augmentation* (CDA) [5], which is effective in extracting environment-dependent context information using only real-time range measurements. We further transform the captured context into a tractable representation that enables *gNodeB* (gNB)-wise NLoS detection in either binary form, termed *hard decision* (HD), or probabilistic form, termed *soft decision* (SD). These decisions are then integrated into novel positioning algorithms designed to meet the accuracy requirement of 6G positioning.

### A. Prior Work

In this subsection, we briefly review existing wireless positioning and NLoS detection methodologies, summarizing their representative approaches and inherent limitations.

1) *Wireless Positioning towards 6G*: Traditional 5G positioning techniques rely heavily on geometry-driven approaches, including time-of-arrival, time-difference-of-arrival, and angle-of-arrival [6]. While these methods perform reliably under *line-of-sight* (LoS) conditions, their efficacy diminishes in NLoS-dominant environments, such as dense urban canyons and complex indoor industrial sites. In these settings, physical obstructions introduce positive biases into range measurements, leading to significant accuracy degradation during the multilateration process [7].

6G has introduced several new features to address the challenges of NLoS propagation. For example, *extremely large-scale multiple-input-multiple-output* (XL-MIMO) has been considered a pivotal enabler, as its superior angular resolution allows for the precise separation of the LoS path from NLoS clutter [8]. Such resolvability allows multipath components to be leveraged as a new spatial degree of freedom, augmenting localization performance rather than degrading it (see, e.g., [9], [10]). Recently, the concept of *movable antenna* (MA) has been introduced, which mechanically adjusts antenna position to mitigate deep fading and optimize channel conditions [11]. The trajectory of MA forms a synthetic aperture with a limited number of antennas, helping resolve and exploit multipath

Sang-Hyeok Kim and Seung-Woo Ko are with Inha University, Incheon 21999, South Korea (e-mail: sanghyeok.kim@inha.edu, swko@inha.ac.kr).

Seung Min Yu is with the Korea Railroad Research Institute, Uiwang 16105, South Korea (e-mail: smyu@krii.re.kr).

Jihong Park is with Singapore University of Technology and Design (SUTD), Singapore 487372 (e-mail: jihong\_park@sutd.edu.sg).

An earlier version of this paper will be presented in part at IEEE Wireless Communications and Networking Conference (WCNC) 2026 [1].

components similar to XL-MIMO [12], [13]. *Reconfigurable intelligent surface* (RIS) is another key technique in 6G, where electromagnetic propagation is intentionally tuned to establish virtual links that bypass blockage [14] or leverage near-field wavefronts to extract additional spatial information [15].

Despite their potential, these techniques often rely on idealized assumptions, such as perfect channel information and continuous phase control, which are frequently untenable in practice due to prohibitive signaling overheads and hardware impairments. Moreover, the substantial hardware investment required for these features poses a significant challenge to the 6G mandate for cost-effective network deployment [16].

2) *AI/ML-Based NLoS Detection & Positioning*: Recent advances in *artificial intelligence* (AI) and *machine learning* (ML) have enabled effective mitigation of the aforementioned NLoS issue. These approaches can be broadly categorized into two methodologies.

The first approach leverages AI/ML models to identify measurements likely captured under NLoS conditions, and subsequently exploits these labels to refine positioning estimates. Classic NLoS detection has been extensively studied under the premise that measurements adhere to predefined probabilistic models, such as Gaussian processes [17] and Gaussian mixture models [18]. However, these models often fail to generalize due to frequent discrepancies with real-world data distributions. In contrast, AI/ML-based frameworks are tailored to capture these latent distributions, effectively learning the complex patterns of the propagation environment embedded in the data.

In [19], for example, a *support vector machine* (SVM)-based NLoS classifier is trained on *channel impulse responses* (CIRs) measured from ultra-wideband transceivers with LoS/NLoS ground-truth labels. A closely related strategy is adopted for MIMO systems in [20], where multiple classifiers, such as SVM, random forest, and neural networks, are trained on *channel state information* (CSI) to distinguish LoS from NLoS conditions. While such supervised approaches are highly effective, they often rely on substantial labeled datasets, motivating efforts to reduce the labeling burden in [21], where LoS-only data samples are used to learn channel embeddings via an autoencoder. NLoS events are then identified through density-based anomaly detection in the learned latent space. Moreover, sequences of consecutive channel-related measurements are often more informative than a single snapshot for NLoS detection, as temporal dynamics can reveal propagation changes and blockage events. To exploit such temporal structure, long short-term memory and transformer-based classifiers are employed in [22] and [23], respectively, both of which are well-suited for handling time-varying patterns. Beyond the above binary decisions, the probabilistic description of NLoS propagation is learned in [24] by training a Real AdaBoost model on labeled CIRs, yielding soft reliability information that can be directly integrated into robust localization.

The second approach directly estimates the target position, bypassing the need for explicit NLoS detection. In this paradigm, NLoS-induced distortions are not viewed as errors to be mitigated, but as informative latent features that characterize the specific propagation environment. By training

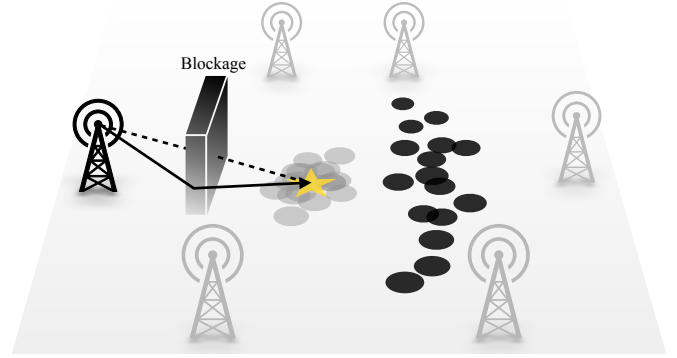


Fig. 1. Graphical illustration of a single snapshot of PELs skewed by a target NLoS gNB. The black circles represent PELs constructed from the target gNB's measurements, while the gray circles represent PELs constructed without it. The yellow star indicates the true UE position.

on these complex signal signatures, the model learns a direct mapping from raw measurements to spatial coordinates, effectively exploiting multipath characteristics as a valuable source of localization information rather than a source of interference.

A representative example is fingerprint-based positioning, where location-dependent fingerprints (e.g., CIR, CSI, or received signal strength) are directly mapped to the target UE's coordinates [25]. With recent advances in AI/ML models, such as transformer-based architectures [26], [27] and emerging large language model paradigm [28], fingerprinting has been actively studied as these models can capture high-dimensional, nonlinear dependencies in rich channel measurements. However, such end-to-end mappings are often considered black-box predictors that are difficult to interpret and analyze, making it nontrivial to connect the learned model to a well-established localization principle and performance guarantees. A recent study in [29] proposes learning a mapping from measurements to the likelihood function, rather than the target location, enabling the use of a maximum likelihood estimator, which is theoretically optimal under standard conditions.

Despite their effectiveness, the practical deployment of the aforementioned AI/ML-based NLoS detection and positioning algorithms remains questionable since they typically require dense site-surveys with ground-truth position labels and often demand frequent re-training as the environment changes.

## B. Contributions

As summarized above, the performance gains of many advanced wireless positioning and NLoS detection techniques come at the cost of extra hardware, significant computation and training overhead, and large-scale real-time data collection, all of which remain difficult to sustain in practice. This challenge becomes even more pronounced toward 6G, which is expected to scale across a wide range of deployment sizes [30], including small indoor areas where such expenses are often impractical. Therefore, it is essential to develop a new technique that can operate effectively while minimally paying these costs.

This work addresses the above issue by proposing a technique termed *CDA-guided NLoS detection* (CDA-ND), which fully utilizes the information embedded in a snapshot of range

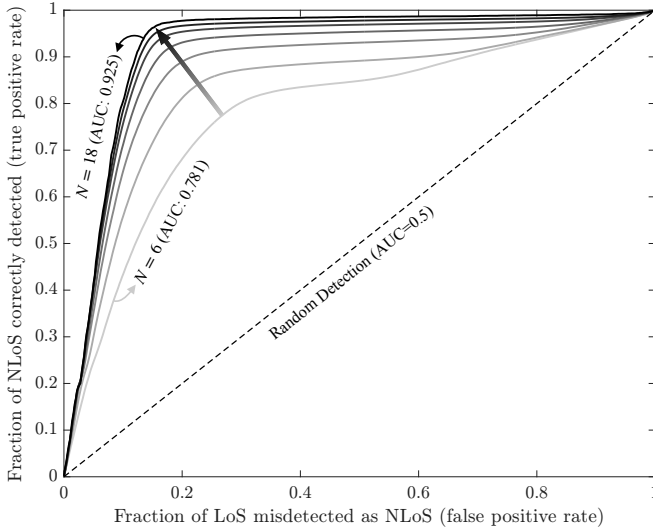


Fig. 2. Receiver operating characteristic curves of the SD output as defined in Sec. IV, under different numbers of gNBs  $N \in \{6, 8, \dots, 18\}$ , in the InF-DH scenario under frequency range 1 (settings in Sec. V-A). Here, “positive” corresponds to NLoS. Darker curves indicate larger  $N$ , with higher AUCs demonstrating better separability between LoS and NLoS links, i.e., higher detection reliability across thresholds.

measurements. Specifically, CDA generates a large set of location candidates by applying multilateration to different subsets of the ranges, defined as *preliminary estimated locations* (PELs). The spatial distribution of these PELs carries informative geometric signature that can be leveraged to determine whether a target gNB is in NLoS. As illustrated in Fig. 1, the PELs can be partitioned into two groups: those constructed using the target gNB’s range measurement (black circles) and those constructed without it (gray circles). When the target gNB is in NLoS, the first group exhibits a directional shift relative to the second group, typically along the direction opposite to the target gNB. This observation enables the design of CDA-ND within the existing communication architecture, without requiring additional hardware or incurring excessive training and labeling overhead.

The key contributions are summarized as follows.

- **CDA-Induced Discriminative Statistics:** The effectiveness of CDA stems from the spatial statistics of the generated PELs, which implicitly encode site-dependent propagation characteristics. Empirically, as the number of participating gNBs increases, the resulting PEL statistics become increasingly stable and discriminative, leading to reliable NLoS detection, as evidenced by the *area under the curve* (AUC) in Fig. 2. Building on this insight, we present our key design components that unleash the full potential of CDA from a positioning perspective.
- **Hard Decision Approach:** To determine whether a target gNB is LoS or NLoS, we introduce the *NLoS evidence vector* (NEV), which summarizes the displacement between the aforementioned PEL groups constructed with and without the target gNB (cf. Fig. 1). Despite its simple form, the NEV provides strong NLoS cues through both its magnitude and direction. We then convert the NEV into a NLoS likelihood score and classify the gNB

as NLoS whenever the score exceeds a predetermined threshold. Building on the HD approach, we develop a novel positioning algorithm that integrates CDA with the identified LoS/NLoS states.

- **Soft Decision Approach:** To quantify a target gNB’s posterior NLoS probability, we develop an SD mapping that converts the NLoS score into a posterior probability by incorporating weak site-survey priors, namely, empirical score samples and the average NLoS probability. This probability mapping is then used to refine the NEV in the HD framework, whose initial construction may rely on incomplete and biased PEL information. Finally, we enhance the positioning stage by assigning reliability-aware weights to PELs according to the SD values of the gNBs involved in their construction, thereby improving robustness and accuracy, particularly in NLoS-dominant environments.
- **Verification on 3GPP-Compliant Dataset:** To validate the effectiveness of the proposed CDA-ND, we conduct extensive simulations on two smart factory scenarios defined in the *3rd generation partnership project* (3GPP) [31], namely *indoor factory-sparse high* (InF-SH) and *indoor factory-dense high* (InF-DH), whose NLoS ratios are 18% and 56%, respectively, under both *frequency range 1* (FR1) and *frequency range 2* (FR2) configurations. We show that CDA-ND achieves high NLoS detection reliability; for example, under FR1, it attains accuracies of 94.70% and 78.04% with HD, and 96.60% and 91.13% with SD, in InF-SH and InF-DH, respectively. Integrating CDA-ND into the positioning stage thus yields substantial accuracy gains, achieving *mean absolute error* (MAE) reductions of 46.60% with HD and 65.99% with SD in the challenging InF-DH scenario.

## II. SYSTEM MODEL

This section describes the positioning network and measurements. We then formulate two types of NLoS detection problems tackled throughout the work.

### A. Scenario and Measurements

Consider a wireless positioning network comprising  $N$  gNBs and a single UE. The set of gNB indices is denoted by  $\mathcal{N} = \{1, \dots, N\}$ . Each gNB is stationary with known *two-dimensional* (2D) coordinates, denoted by  $\mathbf{z}_n \in \mathbb{R}^2$  for  $n \in \mathcal{N}$ . On the other hand, the UE lies at an unknown 2D position  $\mathbf{p} \in \mathbb{R}^2$  within the concerned positioning site, which is to be estimated throughout the work.

We measure *round-trip time* (RTT), denoted by  $\tau_n$ , to obtain a range measurement for each UE-gNB link. It can be obtained by exchanging downlink and uplink reference signals between the UE and gNB  $n$  [32]. This RTT can be translated into an estimated range measurement as  $d_n = \tau_n \frac{c}{2}$ , where  $c \approx 3 \times 10^8$  (m/s) denotes the speed of light. To capture NLoS effects, we define a binary indicator  $\gamma_n \in \{0, 1\}$ , where  $\gamma_n = 1$  if gNB  $n$  is in NLoS and  $\gamma_n = 0$  otherwise. The resultant range measurement  $d_n$  can be expressed as

$$d_n = \|\mathbf{z}_n - \mathbf{p}\| + \gamma_n b_n + w_n, \quad (1)$$

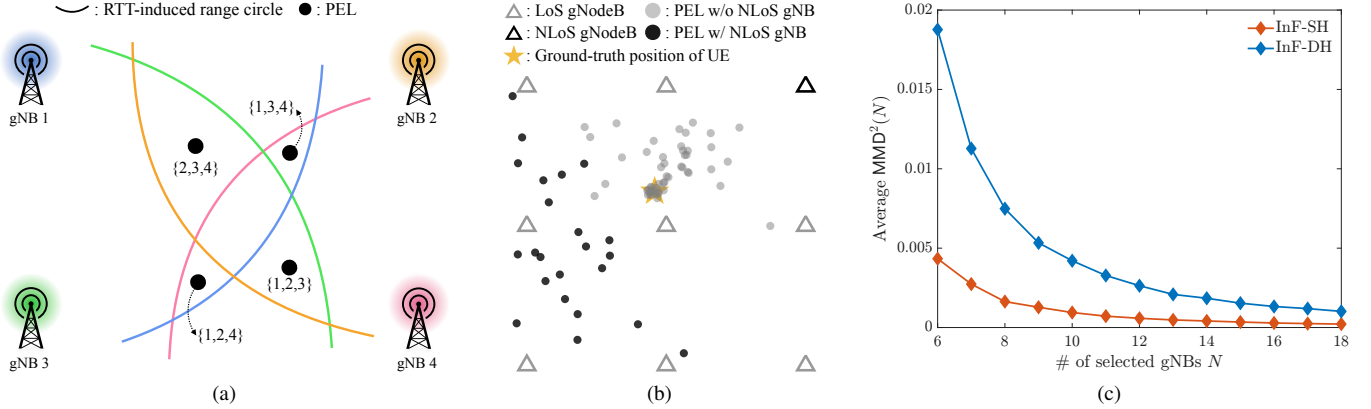


Fig. 3. Illustration of CDA and its implications for NLoS detection. (a) CDA generates multiple PELs by applying multilateration to different subsets of gNB range measurements. (b) When a target gNB is NLoS, the PELs formed with that gNB and those formed without it exhibit a systematic spatial shift, yielding a discriminative geometric NLoS signature in the PEL distribution. (c) The PEL distribution empirically converges as the number of participating gNBs  $N$  increases, quantified by the average squared MMD between the distribution induced by  $N$  and  $(N - 1)$  gNBs.

where  $b_n$  represents the NLoS-induced positive bias and  $w_n$  denotes the ranging noise.

The random quantities  $\gamma_n$ ,  $b_n$ , and  $w_n$  in (1) are governed by latent site-dependent parameters, denoted by  $\Theta$ . The set  $\Theta$  captures factors that are difficult to model or obtain in practice, such as obstacle geometry and material properties [33]. Throughout this work,  $\Theta$  is assumed unknown.

### B. Problem Description

Given the range measurements  $\{d_n\}$  in (1), a baseline for estimating the UE location  $\mathbf{p}$  is multilateration, which infers  $\mathbf{p}$  from the intersection of RTT-induced range circles. However, the latent NLoS states  $\{\gamma_n\}$  introduces unknown positive biases in a subset of range measurements, enlarging the corresponding circles and perturbing their geometric intersections. As a result, multilateration can suffer from large positioning errors. To mitigate the effect, we first aim to identify gNBs that are likely to be in NLoS, and then incorporate this information into the subsequent positioning algorithm. We formulate the following two NLoS detection problems depending on the desired output type.

1) *Hard Decision*: We first determine the NLoS state of each gNB as a binary variable, referred to as a *hard decision* (HD). Ideally, the maximum likelihood detection of NLoS gNBs can be formulated as

$$\{\hat{\gamma}_n\} = \arg \max_{\{\gamma_n\} \in \{0,1\}^N} \Pr(\{d_n\} | \{\gamma_n\}, \Theta). \quad (2)$$

The likelihood in (2) is intractable due to the unknown environmental parameter  $\Theta$ . To address this, we develop a tractable approximation based only on the snapshot range measurement  $\{d_n\}$  and gNB locations  $\{z_n\}$ , which constitutes the main technical contribution in Sec. III.

2) *Soft Decision*: We next assign each gNB an NLoS confidence score (i.e., the posterior NLoS probability), referred to as a *soft decision* (SD), defined by

$$\psi_n = \Pr(\gamma_n = 1 | \{d_n\}, \Theta), \quad \forall n \in \mathcal{N}. \quad (3)$$

Compared with HD, SD provides richer information that can be exploited in downstream tasks. In principle,  $\psi_n$  can be obtained by marginalizing the joint posterior  $\Pr(\{\gamma_n\} | \{d_n\}, \Theta)$ , which remains intractable for the same reason as above. Building on the proposed HD method, we develop a proxy for  $\psi_n$  that leverages site-survey statistics introduced in the sequel, as detailed in Sec. IV.

In the following sections, we present the proposed techniques for both HD and SD, and show how each output can be integrated with positioning algorithm tailored to the corresponding output types.

## III. CDA-GUIDED NLOS DETECTION: HARD DECISION PERSPECTIVE

This section introduces CDA-ND, a key enabler for handling the latent parameters for the HD problem of (2).

### A. Preliminary, Hypothesis, and Overview

We begin by briefly reviewing CDA [5], which generates multiple PELs by exploiting different subsets of gNBs, as illustrated in Fig. 3a. Specifically, selecting  $M$  gNBs from the total of  $N$  yields  $L = \binom{N}{M}$  subsets, denoted by  $\{\mathcal{M}^{(\ell)}\}_{\ell=1}^L$ . For each subset with  $M \geq 3$  (we set  $M = 3$  throughout this paper), the corresponding range measurements are used to compute a PEL as

$$\mathbf{x}^{(\ell)} = g(\{d_n\}_{n \in \mathcal{M}^{(\ell)}}) \in \mathbb{R}^2, \quad \ell \in \{1, \dots, L\}, \quad (4)$$

where  $g(\cdot)$  denotes a conventional multilateration algorithm (e.g., [34]). The complete set of all PELs, visualized as the distribution of circles in Fig. 3a, is defined as

$$\mathcal{X} = \left\{ \mathbf{x}^{(\ell)} \right\}_{\ell=1}^L, \quad (5)$$

which encapsulates diverse aspects of the network geometry, such as potential UE locations, spatial spread, and anisotropy that may hint at blockage directions. For example, as illustrated in Fig. 3b, the PELs exhibit distinct clustering patterns depending on whether the underlying gNB subset is LoS-only

or includes NLoS gNBs. PELs computed from all-LoS subsets (gray circles) form a tightly concentrated, nearly isotropic cluster centered near the ground truth. In contrast, subsets containing NLoS gNBs (black circles) generate clusters that are more anisotropic and spatially dispersed, with their centroid biased away from the NLoS gNB (often in the opposite direction). In other words, the spatial distribution of PELs, denoted by  $U$ , can be interpreted as a proxy for the latent environmental parameter  $\Theta$ . This allows us to revise the likelihood in (2) as

$$\{\hat{\gamma}_n\} = \arg \max_{\{\gamma_n\} \in \{0,1\}^N} \Pr(\{d_n\}, \mathcal{X} \mid \{\gamma_n\}, U). \quad (\text{P1})$$

Assuming a sufficiently large  $N$ , we hypothesize that the ML estimator based on the revised likelihood in P1 behaves asymptotically equivalently to that of the original formulation in (2). This suggests that  $(\{d_n\}, \mathcal{X})$  can be regarded as an asymptotically stable and discriminative set of statistics for NLoS detection.

We empirically investigate the asymptotic property of the PEL spatial distribution as the number of gNBs  $N$  increases, considering two indoor factory scenarios with sparse obstacles (InF-SH) or dense obstacles (InF-DH). Their detailed simulation settings are provided in Sec. V. Let  $\mathcal{X}(N) = \{\mathbf{x}_N^{(\ell)}\}_{\ell=1}^{L(N)}$  denote the set of PELs generated from  $N$  gNBs, where  $L(N) = \binom{N}{3}$ , and view these PELs as samples drawn from the underlying distribution  $U(N)$ . To show the stabilization of  $U(N)$  as  $N$  increases, we quantify the distributional discrepancy between  $U(N)$  and  $U(N-1)$  using the squared maximum mean discrepancy (MMD) [35], which evaluates the distance between the mean embeddings of two distributions in a reproducing kernel Hilbert space. Its empirical squared form is given by

$$\begin{aligned} \text{MMD}^2(N) &= \frac{1}{L(N)^2} \sum_{i,j=1}^{L(N)} \Upsilon(\mathbf{x}_N^{(i)}, \mathbf{x}_N^{(j)}) \\ &+ \frac{1}{L(N-1)^2} \sum_{i,j=1}^{L(N-1)} \Upsilon(\mathbf{x}_{N-1}^{(i)}, \mathbf{x}_{N-1}^{(j)}) \\ &- \frac{2}{L(N)L(N-1)} \sum_{i=1}^{L(N)} \sum_{j=1}^{L(N-1)} \Upsilon(\mathbf{x}_N^{(i)}, \mathbf{x}_{N-1}^{(j)}), \end{aligned} \quad (6)$$

where  $\Upsilon(\mathbf{a}, \mathbf{b}) = \exp(-\varsigma \|\mathbf{a} - \mathbf{b}\|^2)$  represents the Gaussian radial basis function kernel. To ensure a fair and scale-invariant comparison across  $N$ , the kernel bandwidth parameter  $\varsigma$  is set using the median heuristic computed from pairwise squared Euclidean distances among the PELs in  $\mathcal{X}$ .

Fig. 3c shows the statistics of  $\text{MMD}^2(N)$  in (6) over 100 random sequences of gNB selections. In each sequence, gNBs are gradually added from 5 to 18. The UE's location is independently sampled 1,000 times. Two interesting observations can be made. First, the discrepancy between  $U(N-1)$  and  $U(N)$  decreases as  $N$  increases, indicating that the PEL distribution stabilizes and supporting an asymptotic stabilization trend. Second, stabilization is slower in InF-DH than in InF-SH. The denser-obstacle environment exhibits a

richer set of latent propagation factors (captured abstractly by  $\Theta$ ), and thus requires more geometric combinations through more gNBs to sufficiently explain these factors through the induced PEL distribution. Together with the separability trend in Fig. 2, these two observations provide supporting evidence that CDA, given a sufficient number of gNBs, effectively extracts spatial diversity from multiple gNB combinations, enabling us to capture the environment-dependent geometric features using only snapshot measurements.

In the following, our goal is to derive a tractable form of the ML estimator by exploiting the CDA-driven distribution  $U$ . First, a key feature extracted from  $U$  allows us to factorize the likelihood, which reduces the joint ML problem P1 to an independent gNB-wise estimator, as detailed in Sec. III-B. Next, we construct a score function as a surrogate for the likelihood ratio, which enables the design of a simple threshold-based test for HD, as described in Sec. III-C. Finally, we propose a new positioning algorithm that integrates HD into the conventional CDA-based positioning framework, as detailed in Sec. III-D.

### B. Factorization via NLoS Evidence Vector

Problem P1 involves optimizing multiple binary variables  $\{\gamma_n\}$  based on their joint probability mass function. However, deriving this distribution is challenging due to the complex correlations among the variables. To address this challenge, we decompose the joint optimization problem into  $N$  single-variable optimization problems by introducing the following CDA-driven definition.

*Definition 1 (NLoS Evidence Vector (NEV)):* For a given gNB  $n$ , we partition the set of all PELs  $\mathcal{X}$  in (5) into two groups: those constructed using the range measurement  $d_n$  and the remainder, i.e.,

$$\mathcal{X}_n = \{\mathbf{x}^{(\ell)} \in \mathcal{X} \mid n \in \mathcal{M}^{(\ell)}\}, \quad \mathcal{X}_{-n} = \mathcal{X} \setminus \mathcal{X}_n. \quad (7)$$

We then introduce the NEV as the displacement between the representative points of the two groups:

$$\mathbf{r}_n = \mathbf{m}_n - \mathbf{m}_{-n}, \quad (8)$$

where  $\mathbf{m}_n = \text{med}(\mathcal{X}_n)$  and  $\mathbf{m}_{-n} = \text{med}(\mathcal{X}_{-n})$  denote the coordinate-wise medians of  $\mathcal{X}_n$  and  $\mathcal{X}_{-n}$ , respectively.

Fig. 4a illustrates an example of the NEV  $\mathbf{r}_n$  of (8) for a target gNB  $n$  under NLoS. As shown, the NLoS bias shifts the PELs in  $\mathcal{X}_n$  in the direction opposite to gNB  $n$ . Hence, the NEV  $\mathbf{r}_n$  serves as a discriminative feature for identifying whether gNB  $n$  is NLoS. Specifically, a gNB is more likely to be NLoS when  $\mathbf{r}_n$  exhibits the following two key characteristics simultaneously: (i) a sufficiently large magnitude, and (ii) a directional alignment with a reference vector defined as

$$\mathbf{r}_n^0 = \bar{\mathbf{p}} - \mathbf{z}_n, \quad (9)$$

where  $\bar{\mathbf{p}} = \text{med}(\mathcal{X})$  is a pseudo UE location obtainable from the entire PEL set, and gNB  $n$ 's location  $\mathbf{z}_n$  is specified in Sec. II-A. It is important to note that both features should be observed concurrently. Indeed, neither a large magnitude without alignment nor a well-aligned but weak displacement suffices to indicate NLoS. For better intuition, Fig. 4b and

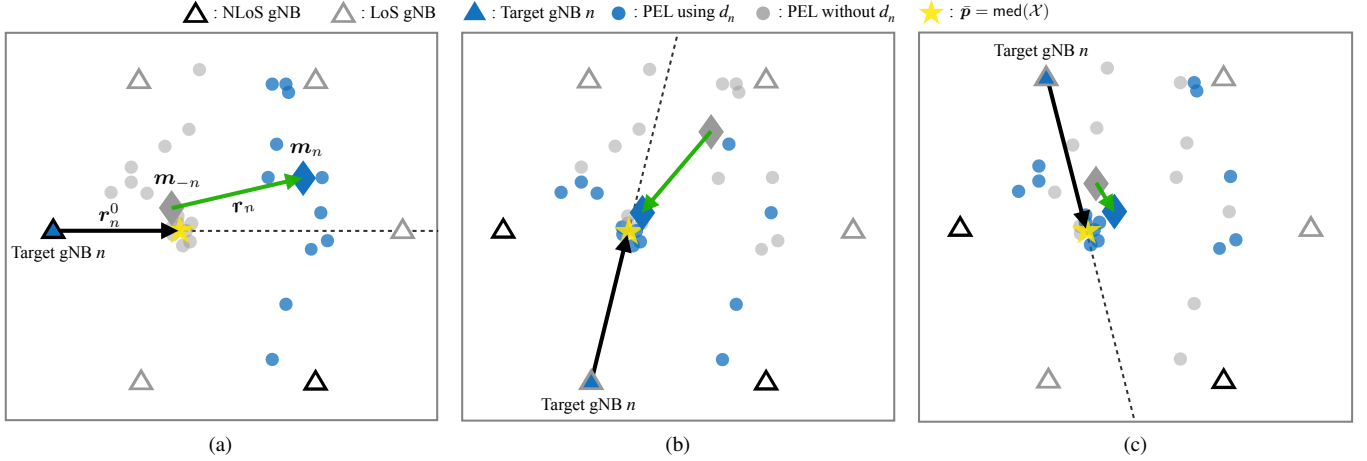


Fig. 4. Examples of the NEV from (8) in a single snapshot across three different target gNB cases: (a) an NLoS case with both sufficient magnitude and directional alignment, (b) a LoS case with sufficient magnitude but directional misalignment, and (c) a LoS case with directional alignment but insufficient magnitude.

Fig. 4c illustrate these two counterexamples: a large but misaligned NEV, and an aligned yet low-magnitude NEV, respectively.

Consequently, the pair  $(\mathbf{r}_n, r_n^0)$  provides sufficient information to infer whether gNB  $n$  is NLoS. This allows the joint likelihood in P1 to be approximately factorized as a product of gNB-wise conditional probabilities:

$$\Pr(\{d_n\}, \mathcal{X} | \{\gamma_n\}, U) \approx \prod_{n \in \mathcal{N}} \Pr(d_n, \mathbf{r}_n | \gamma_n, \mathbf{r}_n^0). \quad (10)$$

Through this factorization, the Problem P1 is transformed into  $N$  independent single-variable tasks, namely:

$$\hat{\gamma}_n = \arg \max_{\gamma \in \{0,1\}} \Pr(d_n, \mathbf{r}_n | \gamma, \mathbf{r}_n^0), \quad (P2)$$

thereby greatly simplifying the decision-making process.

*Remark 1 (Incomplete Reference Vector):* The reference vector  $\mathbf{r}_n^0$  in (9) uses the pseudo location  $\bar{\mathbf{p}} = \text{med}(\mathcal{X})$  instead of the ideal ground-truth position  $\mathbf{p}$  (i.e.,  $\bar{\mathbf{p}} = \mathbf{p}$ ), since it is unknown in practice. While  $\bar{\mathbf{p}}$  is fully implementable and serves as a robust direction proxy for the HD test, it is a static approximation that can be inaccurate when the PEL set is heavily biased by NLoS-contaminated gNBs. This inaccuracy is effectively mitigated within the SD framework in Sec. IV-C, which allows the reference vector to be further refined.

### C. HD: Threshold-Based Test

Assuming that the pseudo location  $\bar{\mathbf{p}}$  in (9) is an effective representative of the ground-truth location  $\mathbf{p}$  (i.e.,  $\bar{\mathbf{p}} = \mathbf{p}$ ), the residual between the estimated distance  $d_n$  and its geometric estimate  $\|\mathbf{r}_n^0\|$  can be expressed as

$$d_n - \|\mathbf{r}_n^0\| = \begin{cases} b_n + w_n & \text{if } \gamma_n = 1, \\ w_n & \text{if } \gamma_n = 0, \end{cases} \quad (11)$$

where the NLoS bias  $b_n$  and the measurement noise  $w_n$  are specified in (1).

Accordingly, Problem P2 can be reformulated as the following threshold test:

$$\frac{f_{b_n+w_n}(d_n - \|\mathbf{r}_n^0\|)}{f_{w_n}(d_n - \|\mathbf{r}_n^0\|)} \underset{\hat{\gamma}_n=0}{\overset{\hat{\gamma}_n=1}{\gtrless}} 1. \quad (12)$$

However, the exact forms of the *probability density functions* (PDFs)  $f_{b_n+w_n}$  and  $f_{w_n}$  are generally unknown, rendering the computation of the likelihood ratio intractable.

To address this limitation, we design a surrogate score function that approximates the log-likelihood ratio by leveraging the NEV  $\mathbf{r}_n$  defined in (8):

$$\rho_n = \left( \frac{\mathbf{r}_n^\top \mathbf{r}_n^0}{\|\mathbf{r}_n^0\|} \right) \sqrt{d_n}. \quad (13)$$

This score comprises two interpretable components. The first term,  $\frac{\mathbf{r}_n^\top \mathbf{r}_n^0}{\|\mathbf{r}_n^0\|}$ , represents the scalar projection of the NEV  $\mathbf{r}_n$  onto the reference vector  $\mathbf{r}_n^0$ , quantifying their directional alignment as discussed in Sec. III-B. The second term,  $\sqrt{d_n}$ , reflects the distance-dependent increase in NLoS probability, which is validated by both well-established channel modeling principles (e.g., 3GPP TR 38.901 [36]) and real-world WiFi measurements (e.g., our prior work in [5]). By combining these two factors, the score function  $\rho_n$  effectively captures the NLoS likelihood: A larger  $\rho_n$  indicates a higher probability that gNB  $n$  is in NLoS. The monotonic relationship between  $\rho_n$  and the NLoS probability is empirically verified, as shown in Fig. 5.

Using the score  $\rho_n$ , we can determine whether gNB  $n$  is NLoS according to the following threshold-based test:

$$\hat{\gamma}_n = \begin{cases} 1 & \text{if } \rho_n \geq \eta. \\ 0 & \text{o.w.} \end{cases} \quad \forall n \in \mathcal{N} \quad (14)$$

Here,  $\eta$  is a decision threshold that balances the trade-off between two performance metrics:

- **Recall:** The ratio of correctly identified NLoS gNBs to the total number of actual NLoS gNBs, reflecting the ability to detect all existing NLoS cases.

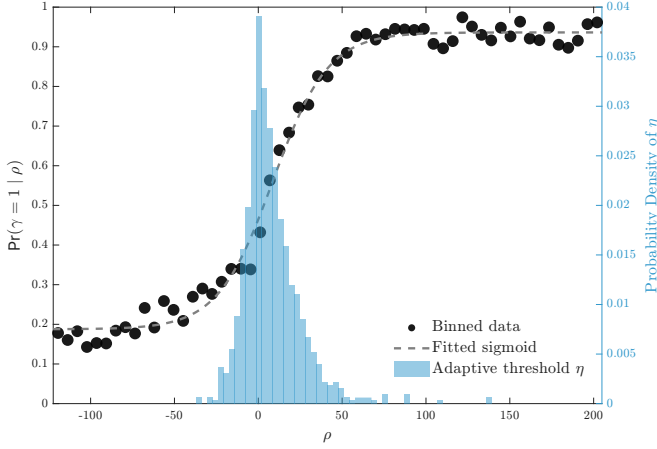


Fig. 5. The empirical NLoS probability with respect to score  $\rho$  in InF-DH under FR1 (details in Sec. V-A), shown to fit a sigmoid curve. Besides, the probability density of the adaptive threshold  $\eta$  is represented by blue histogram.

- **Precision:** The ratio of correctly identified NLoS gNBs to all gNBs classified as NLoS, representing the reliability of NLoS detection results.

Increasing  $\eta$  decreases recall while improving precision. To achieve a robust balance between the two, we adaptively determine  $\eta$  from the distribution of all score values  $\{\rho_n\}_{n \in \mathcal{N}}$  as

$$\eta = \text{med}(\{\rho_n\}) + \lambda \text{med}(\{\text{dev}(\rho_n)\}), \quad (15)$$

where  $\text{dev}(\rho_n) = |\rho_n - \text{med}(\{\rho_n\})|$  and  $\lambda > 0$  is a tunable scaling factor.  $\lambda$  is set to  $\lambda = 1.4$  in InF-SH under FR1,  $\lambda = 1.1$  in InF-SH under FR2, and  $\lambda = 0.5$  in InF-DH under FR1/FR2, and these values are used throughout the numerical evaluations in Sec. V. The first term,  $\text{med}(\{\rho_n\})$ , provides a baseline threshold, corresponding to approximately half of the gNBs being detected as NLoS and defining the nominal recall level. However, this baseline alone may also include several gNBs whose  $\rho_n$  values lie close to the median, which are generally more likely to be LoS rather than NLoS. The second term,  $\text{med}(\{\text{dev}(\rho_n)\})$ , quantifies the overall score dispersion and adjusts the threshold to reduce the false detection of these borderline cases. A larger dispersion indicates that the scores  $\{\rho_n\}$  are more spread out, meaning that potential NLoS gNBs have clearly higher  $\rho_n$  values compared to LoS ones. In such cases, raising the threshold  $\eta$  (via a larger dispersion term) helps focus the detection on the more confident, high-score NLoS gNBs, improving precision without a noticeable loss of recall. Conversely, when the dispersion is small, implying weak separability between LoS and NLoS gNBs, a smaller adjustment keeps  $\eta$  near the baseline to preserve recall.

*Remark 2 (Sigmoid-like NLoS Probability):* Fig. 5 illustrates that the empirical curve of the NLoS probability with respect to  $\rho_n$  closely follows a sigmoid function (dotted line), exhibiting a sharp transition between its lower and upper saturation levels. Here, the transitional range refers to the interval of  $\rho_n$  values where the NLoS probability changes most rapidly, bridging LoS-dominant and NLoS-dominant regions. Interestingly, most threshold values  $\eta$ , represented by the blue histogram, are concentrated near the boundary between the

lower plateau of the sigmoid and this transitional range. This indicates that our adaptive rule favors high recall by capturing nearly all NLoS gNBs, while maintaining reasonable precision by avoiding the region dominated by clear LoS scores. As a result, the threshold design in (15) is well aligned with the empirical score-to-probability relationship.

#### D. Positioning with Hard Decision

Let  $\mathcal{N}_{\text{HD}}$  denote the set of gNBs that remain after excluding those identified as NLoS using HD, i.e.,

$$\mathcal{N}_{\text{HD}} = \{n \in \mathcal{N} \mid \hat{\gamma}_n = 0\}. \quad (16)$$

Although CDA-ND efficiently filters out most NLoS gNBs, the remaining set  $\mathcal{N}_{\text{HD}}$  may still contain undetected NLoS gNBs or LoS gNBs severely corrupted by measurement noise, both of which hinder accurate positioning.

To overcome this limitation, we propose a new CDA-based algorithm that exploits the gNBs in  $\mathcal{N}_{\text{HD}}$  while incorporating two complementary mechanisms, namely, *residual-error* (RE) & *RTT-sum* (RS) filtering, originally introduced in our prior work [5]. These mechanisms jointly enhance the robustness of the location estimate by mitigating the impact of noisy or unreliable measurements within  $\mathcal{N}_{\text{HD}}$ . The detailed, step-by-step procedure of the proposed algorithm is described below.

1) *PEL Selection:* In the first stage, among all PELs,  $\{\mathbf{x}^\ell\} \in \mathcal{X}$  defined in (5), we extract those that are constructed solely from distance measurements of gNBs in  $\mathcal{N}_{\text{HD}}$ , given as

$$\mathcal{X}_{\text{HD}} = \{\mathbf{x}^{(\ell)} \in \mathcal{X} \mid \mathcal{M}^{(\ell)} \subseteq \mathcal{N}_{\text{HD}}\}, \quad (17)$$

where  $\mathcal{M}^{(\ell)}$  denotes the subset of gNBs used to generate PEL  $\mathbf{x}^{(\ell)}$ , with cardinality  $|\mathcal{M}^{(\ell)}| = M$  as specified in Sec. III-A.

2) *Residual-Error Filtering:* In the second stage, we filter the PELs in  $\mathcal{X}_{\text{HD}}$  based on their RE value, defined as

$$u^{(\ell)} = \sum_{n \in \mathcal{M}^{(\ell)}} \left| d_n - \|\mathbf{x}^{(\ell)} - \mathbf{z}_n\| \right|, \quad (18)$$

which quantifies the aggregate discrepancies between the measured distances and the corresponding geometric distances from PEL  $\mathbf{x}^{(\ell)}$  to its associated gNBs. A higher RE value indicates that the PEL is less consistent with the measurements and thus less reliable. To exclude such unreliable PELs, we sort all RE values  $\{u^{(\ell)}\}$  in ascending order and denote the  $\ell_{\text{RE}}$ -th smallest value as  $\bar{u}^{(\ell_{\text{RE}})}$ . We then retain only the PELs whose REs do not exceed this threshold, i.e.,

$$\mathcal{X}_{\text{RE}} = \{\mathbf{x}^{(\ell)} \in \mathcal{X}_{\text{HD}} \mid u^{(\ell)} \leq \bar{u}^{(\ell_{\text{RE}})}\}. \quad (19)$$

3) *RTT-Sum Filtering:* In the third stage, we further filter the PELs in  $\mathcal{X}_{\text{RE}}$  based on their RS values, defined as

$$v^{(\ell)} = \sum_{n \in \mathcal{M}^{(\ell)}} d_n, \quad (20)$$

which represents the total sum of distance measurements used to construct PEL  $\mathbf{x}^{(\ell)}$ . The underlying hypothesis is that a smaller RS value is more likely to be associated with the LoS condition, since NLoS paths typically result in longer RTTs. To retain the PELs most likely to correspond to LoS

propagation, we sort all RS values  $\{v^{(\ell)}\}$  in ascending order and denote the  $\ell_{\text{RS}}$ -th smallest value as  $\bar{v}^{(\ell_{\text{RS}})}$ . The remaining PEL set after RS filtering is given by

$$\mathcal{X}_{\text{RS}} = \left\{ \mathbf{x}^{(\ell)} \in \mathcal{X}_{\text{RE}} \mid v^{(\ell)} \leq \bar{v}^{(\ell_{\text{RS}})} \right\}. \quad (21)$$

4) *Final Location Estimate*: In the final stage, the UE's location is estimated as the median of all PELs that remain after RS filtering, i.e.,

$$\hat{\mathbf{p}}_{\text{HD}} = \text{med}(\mathcal{X}_{\text{RS}}). \quad (22)$$

This strategy, which integrates HD with the subsequent RE&RS filtering, is hereafter termed CDA-ND-RERS (HD).

*Remark 3 (HD vs. RE&RS Filtering)*: Although both HD and RE&RS filtering aim to mitigate the impact of NLoS biases, their specific roles are complementary rather than redundant. HD operates as a gNB-level filtering mechanism, effectively removing dominant NLoS effects, especially in environments where obstacles are spatially clustered (e.g., smart factory). However, because HD excludes all PELs associated with the detected gNB simultaneously, some of the discarded PELs may carry useful geometric information that could improve positioning accuracy. On the other hand, RE&RS filtering functions as a PEL-level mechanism, efficiently addressing moderate NLoS effects arising from small-scale or scattered blockages. Its effectiveness, however, depends on the initial PEL distribution and may degrade when all PELs are biased toward a particular direction. Consequently, the combination of HD and RE&RS filtering offers enhanced robustness across diverse propagation environments, as empirically validated in Sec. V.

#### IV. CDA-GUIDED NLoS DETECTION: SOFT DECISION PERSPECTIVE

This section extends the preceding HD design into an SD approach by estimating the posterior NLoS probability  $\psi_n$  in (3).

##### A. Towards Tractable Soft Decision: Key Idea and Overview

As described in Sec. II-B2,  $\psi_n$  is obtained by marginalizing all variables except  $\gamma_n$  from the joint posterior distribution  $\Pr(\{\gamma_n\} \mid \{d_n\}, \Theta)$ , which is in general intractable due to unknown latent parameters in  $\Theta$ . On the other hand, leveraging the rationale in Sec. III, we derive a tractable approximation of  $\psi_n$ . The key idea is that the scalar score  $\rho_n$  in (13) serves as a sufficient discriminative feature for the NLoS state of gNB  $n$ . Using this score-based representation, we approximate the joint posterior distribution by a gNB-wise factorization:

$$\Pr(\{\gamma_n\} \mid \{d_n\}, \Theta) \approx \prod_{n \in \mathcal{N}} \Pr(\gamma_n \mid \rho_n), \quad (23)$$

where  $\Pr(\gamma_n \mid \rho_n)$  represents the per-gNB posterior conditioned on  $\rho_n$ . This approximation reduces the original high-dimensional marginalization to a univariate posterior inference problem, leading to

$$\psi_n \approx \hat{\psi}_n \triangleq \Pr(\gamma_n = 1 \mid \rho_n), \quad (24)$$

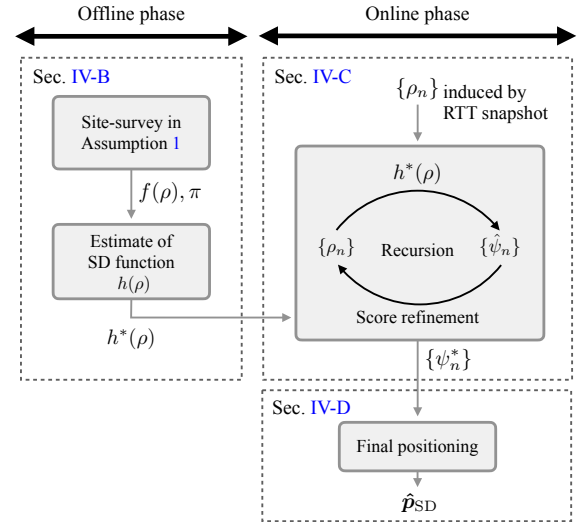


Fig. 6. The pipeline of the SD framework, including SD mapping using weak site-survey prior, recursive score refinement, and final positioning.

which establishes the central link between the SD value and the score  $\rho_n$  used throughout this section.

The remainder of this section consists of three stages. First, assuming the availability of site-survey data, we develop an estimation method that represents (24) via a parametric mapping function in Sec. IV-B. Second, we refine the score  $\rho_n$  by exploiting the recursive relationship between  $\rho_n$  and  $\hat{\psi}_n$  in Sec. IV-C. Finally, we propose a positioning algorithm that integrates the resulting SD mechanism into the standard CDA framework in Sec. IV-D. The overall pipeline is illustrated in Fig. 6.

##### B. Soft-Decision Function

A key challenge in evaluating the approximated SD value  $\hat{\psi}_n$  in (24) is that the stochastic characteristics of the involved variables, namely, the NLoS indicator  $\gamma_n$  and the score  $\rho_n$ , are generally unknown. To make (24) tractable, we assume that weak prior information can be obtained from an online site-survey:

*Assumption 1 (Site-Survey)*: By surveying the positioning environment, we assume the following two site-level statistics are available:

- **Score Samples**: Range measurements are collected over multiple survey locations and converted into scalar scores  $\rho$  using (13). This resulting dataset, denoted by  $\mathcal{Q} \triangleq \{\rho\}$ , provides an empirical basis for estimating the score PDF  $f(\rho)$ .
- **Average NLoS Probability**: During the survey, NLoS events are identified (e.g., via vision-based inspection [37]), enabling estimation of the empirical NLoS probability  $\pi \triangleq \Pr(\gamma = 1)$  by normalizing the number of detected NLoS events by the total number of measurements.

Here, we omit the gNB index in  $\rho$  and  $\pi$  to emphasize that these two statistics characterize the positioning site rather than a specific gNB. Beyond  $f(\rho)$  and  $\pi$ , no additional statistical prior information is assumed.

Next, we define an SD function that converts the score to the posterior probability, given as

$$h(\rho) \triangleq \Pr(\gamma = 1 \mid \rho), \quad (25)$$

where the SD value in (24) can be written as  $\hat{\psi}_n = h(\rho_n)$ . In the following, we explain the procedure of how to find  $h(\rho)$  using the weak site-survey priors in Assumption 1

1) *From Bayes' Rule to a Binary Mixture Model*: Using Bayes' rule, the SD function in (25) can be written as

$$h(\rho) = \frac{\pi f(\rho \mid \gamma = 1)}{f(\rho)}, \quad (26)$$

where the NLoS-conditional score PDF  $f(\rho \mid \gamma = 1)$  is the remaining unknown. Note that the observed score PDF  $f(\rho)$  is formulated via the total-probability decomposition, given as

$$f(\rho) = (1 - \pi)f(\rho \mid \gamma = 0) + \pi f(\rho \mid \gamma = 1). \quad (27)$$

In other words, the observed score PDF is a mixture of the LoS ( $\gamma = 0$ ) and NLoS ( $\gamma = 1$ ) score distributions with mixture weights  $1 - \pi$  and  $\pi$ , respectively.

In the following, we compute  $h(\rho)$  through a two-step approach: (i) estimating a flexible posterior mapping using a constrained *Gaussian mixture model* (GMM), as detailed in IV-B2 and (ii) refining it via a sigmoid fit to better capture tail behavior, as described in IV-B3.

2) *Gaussian Mixture Modeling*: We approximate the site-level PDF  $f(\rho)$  using a  $K$ -component GMM:

$$f(\rho) \approx f_{\text{GMM}}(\rho; \Xi) = \sum_{k=1}^K \alpha_k \varphi(\rho; \mu_k, \sigma_k^2), \quad (28)$$

where  $\varphi(\rho; \mu_k, \sigma_k)$  denotes the Gaussian PDF with mean  $\mu$  and variance  $\sigma^2$ , and

$$\Xi = \{\alpha_k, \mu_k, \sigma_k\}_{k=1}^K, \quad \alpha_k \geq 0, \quad \sum_{k=1}^K \alpha_k = 1. \quad (29)$$

Motivated by the monotonic relationship between  $\rho$  and NLoS probability observed in Remark 2, we enforce an ordering on the component means, namely,  $\mu_1 \leq \mu_2 \leq \dots \leq \mu_K$ . We then partition the components into two groups as  $\{1, \dots, \lceil K/2 \rceil\}$  and  $\{\lceil K/2 \rceil + 1, \dots, K\}$ , which can be interpreted as predominantly LoS- and NLoS-like, respectively. With this partition, we ensure that the total mixture weight assigned to each group matches the surveyed priors  $1 - \pi$  and  $\pi$ . The resultant LoS-conditional and NLoS-conditional score PDFs are given as

$$(1 - \pi)f(\rho \mid \gamma = 0) \approx \sum_{k=1}^{\lceil K/2 \rceil} \alpha_k^* \varphi(\rho; \mu_k^*, (\sigma_k^*)^2), \quad (30a)$$

$$\pi f(\rho \mid \gamma = 1) \approx \sum_{k=\lceil K/2 \rceil + 1}^K \alpha_k^* \varphi(\rho; \mu_k^*, (\sigma_k^*)^2), \quad (30b)$$

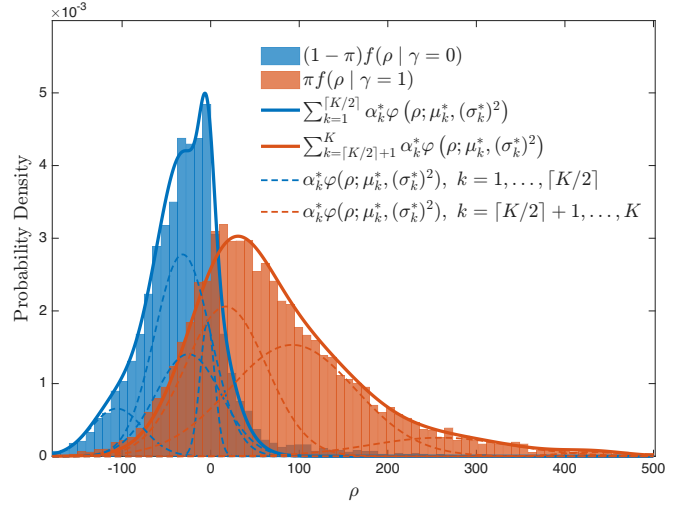


Fig. 7. The empirical PDF of the NLoS score  $\rho$  and its GMM-based modeling in InF-DH under FR1 (details in Sec. V-A). Histograms represent empirical PDF of LoS and NLoS scores weighted by  $1 - \pi$  and  $\pi$ , respectively in (27). All gaussian components in (30) are represented by dotted curves, while its LoS and NLoS mixtures are represented by solid curves.

where  $\Xi^* = \{\alpha_k^*, \mu_k^*, \sigma_k^{*2}\}_{k=1}^K$  is obtained by the following constrained maximum likelihood estimation:

$$\max_{\Xi} \sum_{\rho \in \mathcal{Q}} \ln(f_{\text{GMM}}(\rho; \Xi)) \quad (P3)$$

$$\text{s.t. } \mu_1 \leq \mu_2 \leq \dots \leq \mu_K,$$

$$\sum_{k=1}^{\lceil K/2 \rceil} \alpha_k = 1 - \pi, \quad \sum_{k=\lceil K/2 \rceil + 1}^K \alpha_k = \pi,$$

which can be efficiently solved using a *constrained expectation-maximization* (CEM) algorithm whose details are well summarized in Appendix A. The effectiveness of the algorithm is well visualized in Fig. 7, where the LoS- and NLoS-conditional PDF derived from  $f_{\text{GMM}}(\rho; \Xi^*)$  well aligns with the ground-truth distributions using two weak prior statistics in Assumption 1.

With  $\Xi^*$ , the SD value is approximated by the GMM-induced posterior function, given as

$$h(\rho) \approx \Psi_{\text{GMM}}(\rho; \Xi^*) \triangleq \frac{\sum_{k=\lceil K/2 \rceil + 1}^K \alpha_k^* \varphi(\rho; \mu_k^*, (\sigma_k^*)^2)}{f_{\text{GMM}}(\rho; \Xi^*)}. \quad (31)$$

3) *Sigmoid Fitting*: While  $\Psi_{\text{GMM}}(\rho; \Xi^*)$  is effective near each component's mode, it may be less accurate in the tails due to score-sample sparsity in these regions. This can be overcome by fitting  $\Psi_{\text{GMM}}(\rho; \Xi^*)$  to a generalized sigmoid model:

$$\Psi(\rho; \Phi) = \frac{\phi_1}{1 + \exp(-\phi_2(\rho - \phi_3))} + \phi_4, \quad (32)$$

where  $\Phi = \{\phi_1, \phi_2, \phi_3, \phi_4\}$ . The optimal parameters  $\Phi^*$  are obtained by least-squares fitting over a set of sampled score

points in  $\mathcal{Q}$ :

$$\Phi^* = \arg \min_{\Phi} \sum_{\rho \in \mathcal{Q}} |\Psi_{\text{GMM}}(\rho; \Xi^*) - \Psi(\rho; \Phi)|^2 \quad (33a)$$

$$\text{s.t. } \phi_1 + \phi_4 \leq 1, \quad \phi_1, \phi_2, \phi_4 \geq 0. \quad (33b)$$

Here, the constraint  $\phi_2 \geq 0$  ensures that the mapping is monotonically increasing, while the remaining constraints guarantee a valid probability range of  $[0, 1]$ .

Finally, the SD function in (25) is derived as

$$h^*(\rho) = \Psi(\rho; \Phi^*), \quad (34)$$

where  $h^*$  indicates the best SD function obtained through the above procedure.

### C. Iterative Score Refinement

As recalled in Sec. III-C, the HD score  $\rho_n$  depends on the representative points  $\mathbf{m}_n, \mathbf{m}_{-n}$ , and  $\bar{\mathbf{p}}$ , which are computed by treating all PELs as equally reliable. This unweighted HD process may not match the underlying propagation environment. In particular, when a substantial fraction of PELs are generated using NLoS-contaminated gNBs, the representative points become biased, causing  $\rho_n$  to lose its discriminative feature. Such a bias can lead to incorrect NLoS detection and degrade the subsequent positioning performance.

On the other hand, the SD function in (34) enables us to quantify the reliability of each PEL. Specifically, assuming conditional independence across links, we can define the reliability of PEL  $\ell$  as the probability that all gNBs involved in constructing that PEL are in LoS, namely,

$$\omega^{(\ell)} = \prod_{n \in \mathcal{M}^{(\ell)}} (1 - h^*(\rho_n)). \quad (35)$$

This reliability down-weights PELs constructed from gNBs with high NLoS probabilities.

Using  $\{\omega^{(\ell)}\}$ , we re-estimate the representative points  $\mathbf{m}_n, \mathbf{m}_{-n}$ , and  $\bar{\mathbf{p}}$  as *weighted medians* by minimizing weighted  $L_1$ -distances:

$$\tilde{\mathbf{m}}_n = \arg \min_{\mathbf{m}} \sum_{\{\ell | \mathbf{x}^{(\ell)} \in \mathcal{X}_n \cap \mathcal{X}_{\text{HD}}\}} \omega^{(\ell)} \left\| \mathbf{x}^{(\ell)} - \mathbf{m} \right\|_1, \quad (36)$$

$$\tilde{\mathbf{m}}_{-n} = \arg \min_{\mathbf{m}} \sum_{\{\ell | \mathbf{x}^{(\ell)} \in \mathcal{X}_{-n} \cap \mathcal{X}_{\text{HD}}\}} \omega^{(\ell)} \left\| \mathbf{x}^{(\ell)} - \mathbf{m} \right\|_1, \quad (37)$$

$$\tilde{\mathbf{p}} = \arg \min_{\mathbf{m}} \sum_{\{\ell | \mathbf{x}^{(\ell)} \in \mathcal{X}_{\text{HD}}\}} \omega^{(\ell)} \left\| \mathbf{x}^{(\ell)} - \mathbf{m} \right\|_1, \quad (38)$$

where we restrict the PELs used for re-estimation to the subset  $\mathcal{X}_{\text{HD}}$  specified in (17). This restriction improves robustness by excluding low-confidence PELs that are filtered out in the HD stage. The resultant score, denoted by  $\tilde{\rho}_n$ , is refined as

$$\tilde{\rho}_n = \left( \frac{\tilde{\mathbf{r}}_n^T \tilde{\mathbf{r}}_n^0}{\|\tilde{\mathbf{r}}_n^0\|} \right) \sqrt{d_n}, \quad (39)$$

where

$$\tilde{\mathbf{r}}_n = \tilde{\mathbf{m}}_n - \tilde{\mathbf{m}}_{-n}, \quad \tilde{\mathbf{r}}_n^0 = \tilde{\mathbf{p}} - \mathbf{z}_n. \quad (40)$$

It is worth noting that  $\tilde{\rho}_n$  is recursive: the refined scores can determine the PEL reliabilities through (35), while the reliabilities in turn reshape the representative points in (36)–(38), which subsequently further refine the scores. This motivates an iterative refinement procedure summarized below.

1) *Initialization*: Let  $\tilde{\rho}_n[t]$  denote the gNB  $n$ 's score at iteration  $t$ , initialized with the HD score in (13), i.e.,  $\tilde{\rho}_n[0] = \rho_n$ .

2) *Weight and Score Updates*: Given  $\{\tilde{\rho}_n[t]\}$ , we recompute the PEL weights and representative points via (35)–(38), and then obtain the next iteration score  $\{\tilde{\rho}_n[t+1]\}$  using (39).

3) *Convergence Check*: We iterate until

$$\sum_{n \in \mathcal{N}_{\text{HD}}} (h^*(\tilde{\rho}_n[t+1]) - h^*(\tilde{\rho}_n[t]))^2 \leq \epsilon, \quad (41)$$

where  $\epsilon > 0$  is a predefined threshold. The process terminates when the above condition is satisfied or when the maximum iteration count  $T_{\text{max}}$  is reached.

Upon convergence at iteration  $t^*$ , we obtain the final SD values. For simplicity, we denote them  $\psi_n^*$  by omitting the decoration  $(\hat{\cdot})$ , given as

$$\psi_n^* = \begin{cases} h^*(\tilde{\rho}_n[t^*]) & \text{if } n \in \mathcal{N}_{\text{HD}}, \\ h^*(\rho_n) & \text{if } n \in \mathcal{N} \setminus \mathcal{N}_{\text{HD}}, \end{cases} \quad (42)$$

where gNBs selected for refinement ( $n \in \mathcal{N}_{\text{HD}}$ ) use the refined score  $\tilde{\rho}_n[t^*]$  as an input of the optimal function  $h^*$  in (25), while the remaining gNBs use the original score  $\rho_n$ .

### D. Positioning with Soft Decision

We exploit the above SD values  $\{\psi_n^*\}$  to compute the UE location more accurately by taking the weighted median of  $\mathcal{X}_{\text{RS}}$ , given as

$$\hat{\mathbf{p}}_{\text{SD}} = \arg \min_{\mathbf{p} \in \mathbb{R}^2} \sum_{\{\ell | \mathbf{x}^{(\ell)} \in \mathcal{X}_{\text{RS}}\}} \omega^{*(\ell)} \left\| \mathbf{x}^{(\ell)} - \mathbf{p} \right\|_1, \quad (43)$$

where

$$\omega^{*(\ell)} = \prod_{n \in \mathcal{M}^{(\ell)}} (1 - \psi_n^*), \quad (44)$$

and the RE&RS filtered PEL subset  $\mathcal{X}_{\text{RS}}$  is specified in (21). This strategy is hereafter termed CDA-ND-RERS (SD).

*Remark 4 (Role of SD for Positioning)*: Compared with HD-based positioning in Sec. III, SD helps further improve positioning accuracy by replacing the unweighted median in (22) to a weighted median. Although the HD combined with RE&RS filtering can remove gNBs and PELs that are likely NLoS-corrupted (Remark 3), it still assigns equal importance to all remaining PELs in  $\mathcal{X}_{\text{RS}}$ . Consequently, the unweighted median in (22) may be suboptimal, particularly in NLoS-dominant environments where the retained PELs can have markedly different levels of reliability. On the other hand, SD differentiates the contribution of each PEL through its reliability weight  $\omega^{*(\ell)}$ , thereby yielding a weighted median that better captures the true representative point of the filtered PEL set. This reliability-aware computation directly translates into improving positioning accuracy, as empirically validated in Sec. V.

Actual	NLoS	HD: 90.29 % SD: 94.12 %	HD: 9.71 % SD: 5.88 %
	LoS	HD: 4.29 % SD: 2.87 %	HD: 95.71 % SD: 97.13 %
		NLoS	LoS
Predicted			
(a) InF-SH FR1.			
Actual	NLoS	HD: 82.83 % SD: 87.63 %	HD: 17.17 % SD: 12.36 %
	LoS	HD: 10.50 % SD: 9.66 %	HD: 89.50 % SD: 90.34 %
		NLoS	LoS
Predicted			
(b) InF-SH FR2.			
Actual	NLoS	HD: 73.24 % SD: 97.19 %	HD: 26.76 % SD: 2.81 %
	LoS	HD: 15.76 % SD: 16.70 %	HD: 84.24 % SD: 83.30 %
		NLoS	LoS
Predicted			
(c) InF-DH FR1.			
Actual	NLoS	HD: 73.48 % SD: 97.72 %	HD: 26.52 % SD: 2.28 %
	LoS	HD: 15.03 % SD: 15.72 %	HD: 84.97 % SD: 84.38 %
		NLoS	LoS
Predicted			
(d) InF-DH FR2.			

Fig. 8. Confusion matrix of binary NLoS detection results where HD and SD denote HD-based and SD-based results, respectively.

TABLE I  
RANGE-MEASUREMENT ERROR STATISTICS (MEAN/STD) FOR EACH SCENARIO-CARRIER CONFIGURATION.

Frequency Range	InF-SH ( $\pi = 0.18$ )				InF-DH ( $\pi = 0.56$ )			
	LoS [m]		NLoS [m]		LoS [m]		NLoS [m]	
	Mean	Std	Mean	Std	Mean	Std	Mean	Std
FR1	1.48	5.92	26.06	20.08	4.00	14.04	25.13	19.24
FR2	4.35	48.44	64.69	318.11	3.23	11.62	26.84	22.71

## V. NUMERICAL RESULTS

### A. Simulation Setup

We validate CDA-ND using the publicly available 3GPP-compliant positioning dataset in [31]. We consider two indoor factory scenarios: InF-SH and InF-DH, representing LoS-dominant and NLoS-dominant environments whose NLoS ratios  $\pi$  are 0.18 and 0.56, respectively. Following the standard deployments, we use  $N = 18$  gNBs in both scenarios. The factory area is  $300\text{m} \times 150\text{m}$  for InF-SH and  $120\text{m} \times 60\text{m}$  for InF-DH.

For each UE realization, we use the dataset-provided gNB coordinates  $\{z_n\}$ , the binary LoS/NLoS labels  $\{\gamma_n\}$ , and RTT-based range measurements  $\{d_n\}$ , where  $d_n$  is obtained by averaging the downlink- and uplink range estimates from reference signals. Two FR configurations are considered: FR1 with a 3.5 GHz carrier and FR2 with a 28 GHz carrier, both with 100 MHz bandwidth. All other simulation settings, including the 3GPP standard-based wireless channel generation, the reference signal configurations, and scenario-specific parameters, follow the dataset generation procedure in [31]. The resulting range-measurement statistics of each configuration are summarized in Table I.

For each scenario-frequency configuration, the dataset provides 100 spatially consistent scenario instantiations (with spatially consistent channels and NLoS maps) and 10 UE drops per instantiation, resulting in 1000 UE realizations per configuration. We partition these 1000 UE realizations into 10 subsets: one subset is used to evaluate the NLoS detection and positioning performance, while the remaining nine subsets are used to construct the SD mapping function in Sec. IV-B. We repeat this process 10 times by changing the evaluation, thereby performing 10-fold cross-validation.

TABLE II  
NLoS DETECTION PERFORMANCE COMPARISON.

Mode	Metric	InF-SH		InF-DH	
		FR1	FR2	FR1	FR2
Hard Decision	Recall [%]	90.29	82.83	73.24	73.48
	Precision [%]	81.79	63.84	85.72	86.14
	Accuracy [%]	94.76	88.28	78.04	78.54
	AUC	0.967	0.918	0.842	0.836
Soft Decision	Recall [%]	94.12	87.63	97.19	97.72
	Precision [%]	87.48	66.99	88.26	88.83
	Accuracy [%]	96.60	89.84	91.13	91.84
	AUC	0.985	0.946	0.925	0.936

### B. NLoS Detection Performance

We evaluate gNB-wise LoS/NLoS detection against the dataset-provided ground-truth labels. Throughout this section, the primary objective is to reliably identify NLoS-contaminated gNBs, since leaving an NLoS link in the usable set can inject an unknown positive bias  $b_n$  into the range model (1) and severely distort geometry-driven localization.

We use the following metrics to summarize detection performance in Table II.

- *Recall*: The number of gNBs correctly detected as NLoS, normalized by the total number of truly NLoS gNBs.
- *Precision*: The number of gNBs correctly detected as NLoS normalized by the total number of gNBs detected as NLoS.
- *Accuracy*: The fraction of gNBs whose LoS/NLoS states are correctly classified, i.e., the number of correctly classified gNBs normalized by the total number of gNBs.
- *AUC*: We report the AUCs of the raw score  $\rho_n$  in (13) for HD and the final SD value  $\psi_n^*$  in (42) for SD.

We also provide the confusion matrices in Fig. 8a–8d, where the NLoS threshold follows (15) for HD and is set to 0.5 for SD.

In general, both HD and SD modes provide reliable performance across all scenario-frequency configurations, while several interesting observations are made.

1) *HD vs. SD*: HD relies on unweighted representative points to form  $r_n$  and  $r_n^0$  (Sec. III-B), hence its score  $\rho_n$  in (13) can lose discriminability when many PELs are affected by NLoS-contaminated gNBs (Remark 1). SD mitigates this issue by incorporating weak site-survey priors (Assumption 1) and applying the reliability-weighted refinement in Sec. IV-C,

which consistently improves separability. For example, Table II shows that the AUC increases from 0.842 to 0.925 in InF-DH FR1 when moving from HD to SD, together with the corresponding accuracy improvements from 78.04% to 91.13% (InF-DH FR1).

Beyond AUC, SD is intentionally tuned to strengthen the primary objective of capturing NLoS links, even at the cost of occasionally misclassifying some LoS links. This behavior is most visible in Fig. 8c–8d: SD drastically reduces the cases where a truly NLoS gNB is mistakenly treated as LoS, as shown in the reductions from 26.76% to 2.81% in FR1 and from 26.52% to 2.28% in FR2. As a result, SD captures nearly all NLoS-contaminated gNBs (about 97% coverage of NLoS links). In comparison, the accompanying increase in misclassifying LoS links remains marginal (less than 1% reduction in the fraction of truly LoS links kept as LoS), which is an acceptable trade-off for positioning.

The rationale is as follows. If an NLoS-contaminated gNB is left in the usable set, its unknown bias  $b_n$  in (1) can dominate subsequent geometry-driven localization (e.g., LS multilateration). In contrast, when a LoS gNB is excluded, the primary effect is a reduced number of usable links, which is relatively less harmful when sufficient gNB diversity remains and CDA provides redundant geometric combinations. Moreover, since the observed ranging error is a composite of  $w_n$  and  $\gamma_n b_n$  in (1), LoS links that are excluded by SD are often large-noise outliers (Table I), so discarding them does not necessarily degrade positioning and can even improve robustness under heterogeneous measurement quality.

2) *FR1 vs. FR2*: The difference between FR1 and FR2 is largely driven by ranging quality differences in Table I. In particular, in InF-SH the LoS ranging standard deviation increases from 5.92 m in FR1 to 48.44 m in FR2, which increases the likelihood that noise-driven outliers produce NLoS-like score patterns in (13). Consistently, Table II shows that the HD AUC decreases from 0.967 to 0.918 and the accuracy decreases from 94.76% to 88.28% when moving from FR1 to FR2 in InF-SH. This trend is also reflected in Fig. 8a–8b, where the fraction of truly LoS gNBs excluded as NLoS (bottom-left cell) increases from 4.29% to 10.50% in HD.

In InF-DH, NLoS bias effects are dominant in both FR1 and FR2 (Table I), and SD focuses on reducing NLoS misses via score refinement-based PEL re-weighting. Accordingly, Table II shows that SD maintains high AUC values around 0.93 for both FR1 and FR2, and Fig. 8c–8d shows that the missed-NLoS fractions remain around a few percent under SD.

3) *InF-SH vs. InF-DH*: In InF-SH, the NLoS ratio  $\pi$  is relatively low. Consequently, the HD score  $\rho_n$  in (13) already captures the underlying geometry reasonably well even without SD refinement. For instance, Table II reports high AUC values under HD, namely 0.967 in FR1 and 0.918 in FR2, together with accuracies of 94.76% and 88.28%, respectively. In this LoS-dominant regime, SD provides an additional but moderate gain, e.g., the AUC increases to 0.985 and 0.946 in FR1 and FR2, respectively (Table II), which mainly corrects borderline cases through reliability-aware refinement.

On the other hand, InF-DH has a higher NLoS ratio  $\pi$

TABLE III  
HYPERPARAMETER SETTINGS FOR RE&RS FILTERING.

Method	Parameter	InF-SH		InF-DH	
		FR1	FR2	FR1	FR2
CDA-RERS	$\ell_{RE}/L$	0.63	0.53	0.15	0.15
	$\ell_{RS}/L$	0.36	0.26	0.08	0.08
CDA-ND-RERS (HD)	$\ell_{RE}/L$	0.88	0.85	0.23	0.23
	$\ell_{RS}/L$	0.83	0.75	0.1	0.1
CDA-ND-RERS (SD)	$\ell_{RE}/L$	0.98	0.96	0.30	0.30
	$\ell_{RS}/L$	0.96	0.94	0.15	0.15

than InF-SH, so a substantial fraction of PELs are generated from subsets containing NLoS-contaminated links, making the representative points and the resulting HD score  $\rho_n$  more vulnerable to bias (Remark 1). This is reflected in Table II, where the HD AUC drops to 0.842 in FR1 and 0.836 in FR2, with accuracies of 78.04% and 78.54%. In this NLoS-dominant regime, SD becomes particularly effective: Table II shows that the AUC increases to 0.925 in FR1 and 0.936 in FR2, and Fig. 8c–8d confirms that the missed-NLoS fractions are reduced from about 26% in HD to about 2% in SD.

### C. Positioning Performance

Positioning performance is evaluated in terms of the 2D error under the scenario–frequency configurations as established in Sec. V-A. Fig. 9 and Fig. 10 show the *cumulative distribution functions* (CDFs) of positioning error for FR1 and FR2, respectively, while Table IV reports the mean, median, and 95th percentile errors.

The compared methods are grouped into benchmarks and the proposed methods as follows. *Benchmarks*:

- *Least-squares (LS)*: Standard multilateration using all gNB measurements in  $\mathcal{N}$  [34].
- *CDA-RERS*: RE&RS filtering in (18)–(20) applied to the full PEL set  $\mathcal{X}$ , followed by  $\text{med}(\cdot)$  of the retained PELs [5].
- *LS-ND (HD)*: LS applied to the LoS-identified gNB subset  $\mathcal{N}_{HD}$  in (16).
- *CDA-ND (HD)*: Unweighted median over  $\mathcal{X}_{HD}$  in (17).
- *LS-ND (SD)*: Weighted LS applied to  $\mathcal{N}_{HD}$  with per-gNB weight  $(1 - \psi_n^*)$ , where  $\psi_n^*$  is given in (42).
- *CDA-ND (SD)*: Reliability-aware weighted median over  $\mathcal{X}_{HD}$  using  $\omega^{*(\ell)}$  in (44).

*Proposed*:

- *CDA-ND-RERS (HD)*: Form  $\mathcal{X}_{HD}$  in (17), apply RE&RS filtering to obtain  $\mathcal{X}_{RS}$  in (21), and compute  $\text{med}(\mathcal{X}_{RS})$ , yielding  $\hat{p}_{HD}$  in (22).
- *CDA-ND-RERS (SD)*: Same as CDA-ND-RERS (HD), but replacing  $\text{med}(\mathcal{X}_{RS})$  with the reliability-aware weighted median over  $\mathcal{X}_{RS}$ , yielding  $\hat{p}_{SD}$  in (43).

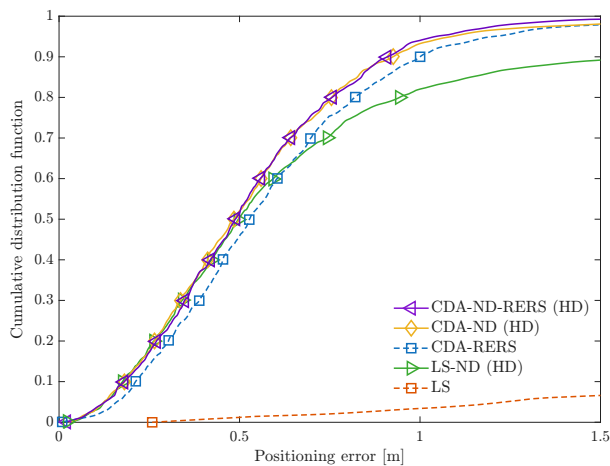
The RE&RS retained ratios (reported as  $\ell_{RE}/L$  and  $\ell_{RS}/L$ ) are given in Table III. For the SD mapping function, we use the GMM decomposition in (28) with  $K = 8$ ; the iterative refinement in Sec. IV-C uses  $\epsilon = 10^{-3}$  and  $T_{\max} = 25$ .

Fig. 9 reports the FR1 results. In the LoS-dominant InF-SH case, Fig. 9a–9b shows that CDA-based estimators concentrate

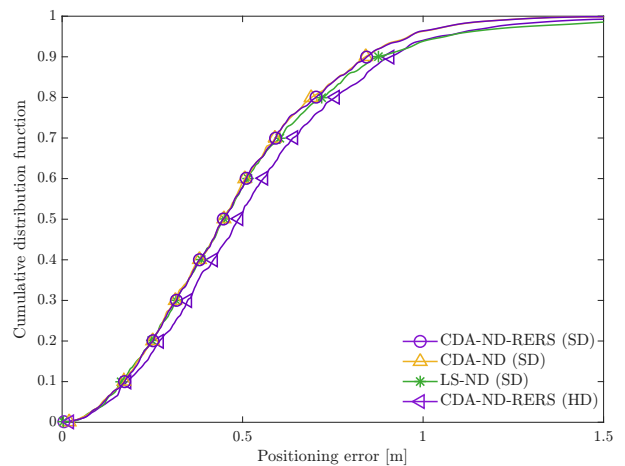
TABLE IV

POSITIONING ERROR STATISTICS (m) FOR EACH SCENARIO–FREQUENCY CONFIGURATION. THE PROPOSED METHODS ARE HIGHLIGHTED IN BOLD&gt;.

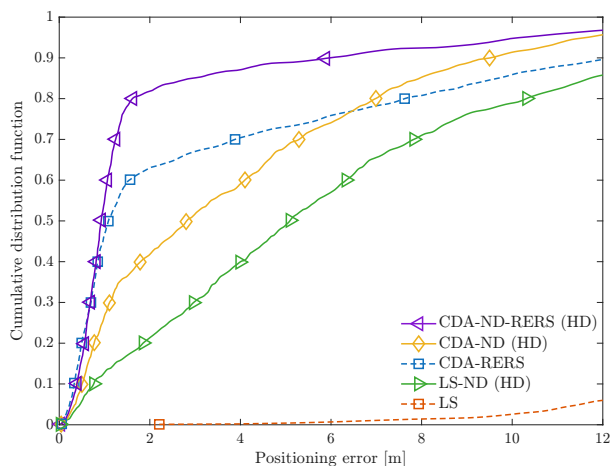
Mode	Method	InF-SH								InF-DH							
		FR1				FR2				FR1				FR2			
		Mean	Std	Med	95th	Mean	Std	Med	95th	Mean	Std	Med	95th	Mean	Std	Med	95th
w/o	LS	8.07	5.53	6.90	18.03	20.43	40.41	11.34	69.50	23.06	9.24	21.60	38.80	22.74	7.98	22.13	36.10
CDA-ND	CDA-RERS	0.60	0.45	0.53	1.21	1.19	1.83	0.72	3.76	3.97	5.51	1.08	16.08	3.73	5.42	1.08	16.29
Hard Decision	LS-ND (HD)	0.85	1.53	0.49	2.90	2.06	3.84	0.77	8.25	7.09	7.90	5.10	21.37	6.28	6.47	4.59	16.79
	CDA-ND (HD)	0.55	0.40	0.48	1.09	1.05	1.72	0.62	3.75	4.01	4.03	2.81	11.72	4.13	4.48	2.69	12.14
	<b>CDA-ND-RERS (HD)</b>	0.53	0.33	0.48	1.05	0.88	1.32	0.58	2.27	2.12	3.59	0.92	10.23	2.32	4.04	0.97	12.15
Soft Decision	LS-ND (SD)	0.53	0.75	0.45	1.06	0.98	2.35	0.66	2.41	2.53	5.66	1.09	9.11	2.25	4.18	1.06	8.99
	CDA-ND (SD)	0.48	0.27	0.45	0.97	0.68	0.47	0.57	1.49	1.52	2.74	0.77	6.08	1.62	3.19	0.77	6.76
	<b>CDA-ND-RERS (SD)</b>	0.48	0.27	0.45	0.97	0.67	0.47	0.57	1.49	1.35	2.78	0.77	5.56	1.52	3.07	0.79	6.07



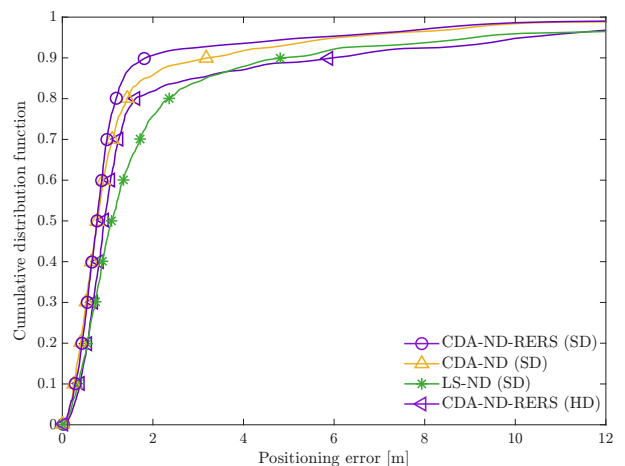
(a) HD-based positioning in InF-SH scenario.



(b) SD-based positioning in InF-SH scenario.



(c) HD-based positioning in InF-DH scenario.



(d) SD-based positioning in InF-DH scenario.

Fig. 9. Positioning performance under FR1. The performance is reported in terms of CDF of the positioning error.

in the sub-meter regime, whereas LS-ND (HD) exhibits a pronounced right shift with a long tail. Table IV quantifies this contrast: LS has a MAE of 8.07 m, while CDA-RERS reduces it to 0.60 m and the proposed CDA-ND-RERS reaches 0.53 m in (HD) and 0.48 m in (SD). This small HD–SD gap (0.53 m vs. 0.48 m) matches the NLoS-detection reliability in Sec. V-B: in InF-SH FR1, HD already attains accuracy 94.76 % and AUC 0.967, and SD increases them to 96.60 %

and 0.985 in Table II. This behavior is also consistent with the PEL stabilization trend in Fig. 3c, which is faster in InF-SH, reducing the need for additional SD-based refinement beyond gNB-level exclusion of HD.

In the NLoS-dominant InF-DH scenario under FR1, Fig. 9c shows that LS remains unreliable even after the HD-based gNB-level exclusion, and that combining ND with PEL-level RE&RS filtering yields a substantial improvement. Specifi-

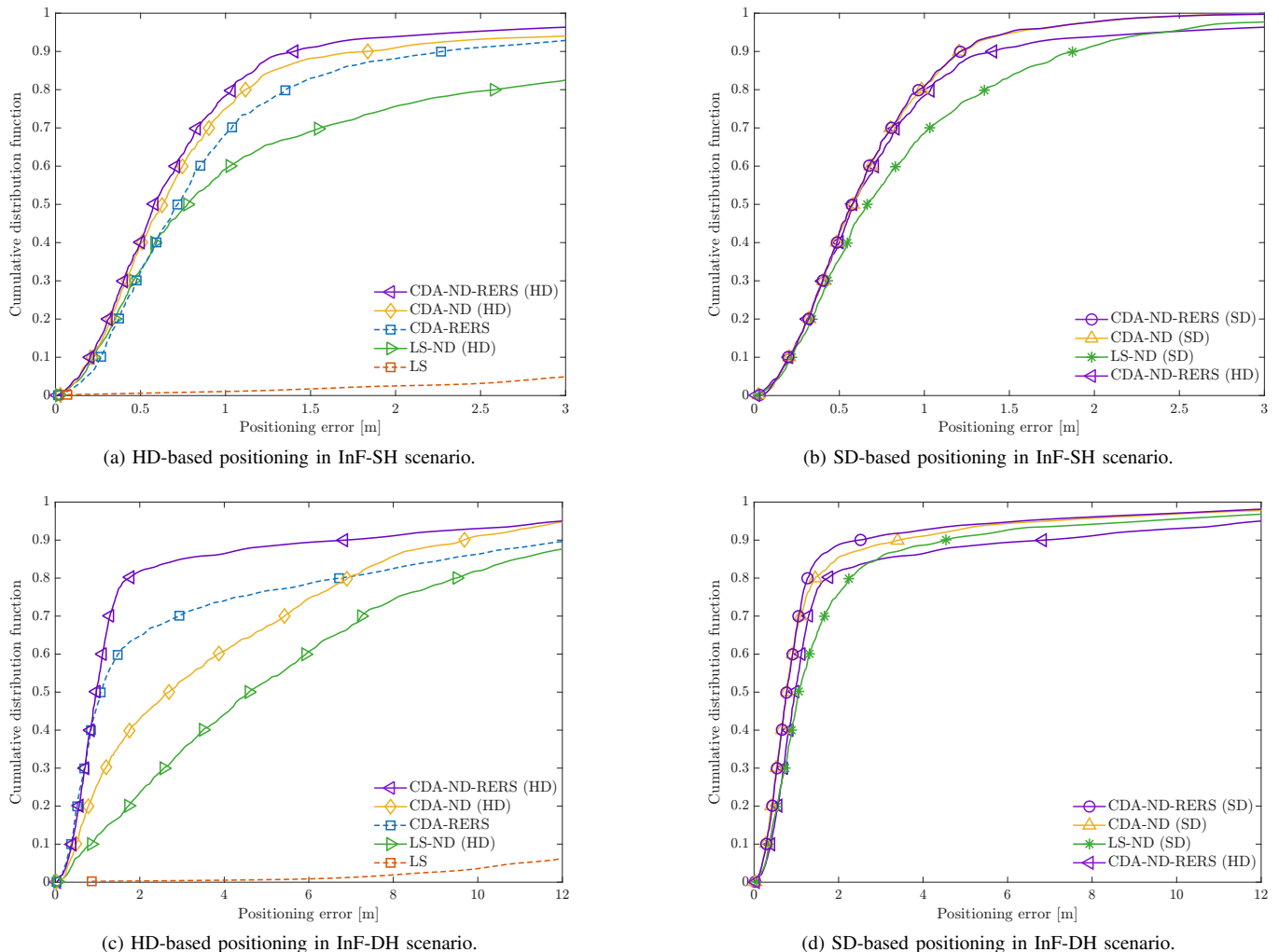


Fig. 10. Positioning performance under FR2. The performance is reported in terms of CDF of the positioning error.

cally, Table IV shows that LS has a MAE of 23.06 m and LS-ND (HD) still yields 7.09 m, whereas CDA-ND-RERS (HD) reduces it to 2.12 m. Fig. 9d further indicates a pronounced tail improvement under SD-based processing; correspondingly, the 95th percentile decreases from 10.23 m to 5.56 m and the MAE decreases from 2.12 m to 1.35 m when moving from CDA-ND-RERS (HD) to CDA-ND-RERS (SD) in Table IV. This gain is consistent with the detection results in InF-DH FR1, where Table II shows that SD increases the NLoS detection accuracy from 78.04% to 91.13% and the AUC from 0.842 to 0.925. InF-DH under FR2 follows the same pattern.

Fig. 10 reports the FR2 results. In InF-SH FR2, Fig. 10a shows a larger performance degradation than in FR1 (Fig. 9a). Table IV summarizes the gap for the proposed method: CDA-ND-RERS (HD) increases from 0.53 m to 0.88 m, whereas it increases from 0.48 m to 0.67 m in CDA-ND-RERS (SD). This is consistent with NLoS detection performance and ranging statistics: in InF-SH, FR2 has weaker detection separability than FR1 (HD AUC 0.967  $\rightarrow$  0.918 in Table II) and much larger LoS dispersion (LoS standard deviation 5.92 m  $\rightarrow$  48.44 m in Table I).

In InF-DH, the FR1/FR2 gap is modest. This is also reflected in Fig. 9–Fig. 10, where the InF-DH SD-based CDFs in Fig. 9d and Fig. 10d exhibit similar shapes. Numerically, CDA-ND-RERS (SD) achieves MAEs of 1.35 m in FR1 and 1.52 m in FR2, with 95th percentiles of 5.56 m and 6.07 m, respectively (Table IV).

Finally, Fig. 9–Fig. 10 show that gNB-level exclusion and PEL-level RE&RS filtering are complementary, and that SD further improves robustness by applying the PEL-weighted median in (43).

## VI. CONCLUDING REMARKS

This work has developed CDA-ND, a novel NLoS detection algorithm that exploits discriminative geometric signatures manifested in CDA-generated PELs, which are constructed solely from real-time gNB-UE range measurements. These signatures are compactly captured by a single vector, termed NEV, which enables a tractable HD detector that operates online. When weak site-survey priors are available, the framework naturally extends to the SD mode that quantifies posterior NLoS probabilities. Both HD and SD outputs are seamlessly

integrated into CDA-based positioning algorithms, whose effectiveness is extensively validated through simulation studies on a 3GPP-compliant dataset.

The current work can be extended in several directions. First, although this work focuses on positioning, the CDA-ND features can benefit a broader range of 6G tasks, such as LoS/NLoS-aware beamforming and link adaptation. Second, gNBs identified as NLoS implicitly provide hints on dominant reflections. Leveraging these hints to infer coarse reflection-point locations could complement vision-based sensing and help mitigate drift. Last, integrating CDA-ND with emerging 6G technologies, such as MA and RIS, will be another interesting direction.

#### APPENDIX A CONSTRAINED EXPECTATION-MAXIMIZATION

To tackle P3, we propose a *constrained expectation-maximization* (CEM) algorithm that explicitly enforces the site-survey prior  $\pi$  in P3. Let the score-sample set be  $\mathcal{Q} \triangleq \{\rho_q\}_{q=1}^Q$  where  $Q \triangleq |\mathcal{Q}|$ , and define the GMM in (28) at iteration  $t$  as

$$f_{\text{GMM}}(\rho; \Xi[t]) \triangleq \sum_{k=1}^K \alpha_k[t] \varphi(\rho; \mu_k[t], (\sigma_k[t])^2), \quad (45)$$

where  $\Xi[t] \triangleq \{\alpha_k[t], \mu_k[t], \sigma_k[t]\}_{k=1}^K$ .

The iterative steps of the proposed CEM are as follows:

- *Expectation Step (E-step)*: Given the current parameters  $\Xi[t]$ , we evaluate the responsibility  $\zeta_{q,k}[t]$ , i.e., the posterior probability that the observation  $\rho_q$  originates from the  $k$ -th Gaussian component:

$$\zeta_{q,k}[t] = \frac{\alpha_k[t] \varphi(\rho_q; \mu_k[t], (\sigma_k[t])^2)}{f_{\text{GMM}}(\rho_q; \Xi[t])}. \quad (46)$$

The aggregate responsibility for each component is then computed as

$$S_k[t] = \sum_{q=1}^Q \zeta_{q,k}[t], \quad k \in \{1, \dots, K\}. \quad (47)$$

- *Maximization Step (M-step)*: The parameters are updated to  $\Xi[t+1]$  to maximize the log-likelihood in P3 while enforcing its constraints. First, the means and standard deviations are updated as in the standard EM:

$$\mu_k[t+1] = \frac{1}{S_k[t]} \sum_{q=1}^Q \zeta_{q,k}[t] \rho_q, \quad (48a)$$

$$\sigma_k[t+1] = \sqrt{\frac{1}{S_k[t]} \sum_{q=1}^Q \zeta_{q,k}[t] (\rho_q - \mu_k[t+1])^2}. \quad (48b)$$

Next, to satisfy the monotonic constraint in P3, we sort the updated means in ascending order such that  $\mu_1[t+1] \leq \mu_2[t+1] \leq \dots \leq \mu_K[t+1]$ , and permute  $\{\alpha_k[t], \sigma_k[t+1], S_k[t]\}$  accordingly to keep each component consistent after re-indexing. Finally, letting  $k^* = \lceil K/2 \rceil$  (as used in Sec. IV-B2), we enforce the

prior-mass constraints in P3 by renormalizing the mixing weights within each partition:

$$\alpha_k[t+1] = \begin{cases} (1 - \pi) \frac{S_k[t]}{\sum_{m=1}^{k^*} S_m[t]} & \text{if } 1 \leq k \leq k^*, \\ \pi \frac{S_k[t]}{\sum_{m=k^*+1}^K S_m[t]} & \text{if } k^* < k \leq K. \end{cases} \quad (49)$$

- *Convergence Check*: The iterations stop when

$$\left| \sum_{q=1}^Q \ln f_{\text{GMM}}(\rho_q; \Xi[t+1]) - \sum_{q=1}^Q \ln f_{\text{GMM}}(\rho_q; \Xi[t]) \right| \leq \epsilon, \quad (50)$$

where  $\epsilon > 0$  is a predefined threshold (or when a maximum iteration count is reached).

Upon convergence at  $t^*$ , the algorithm outputs the estimated parameters  $\Xi^* \triangleq \Xi[t^*]$ .

#### REFERENCES

- [1] S.-H. Kim, S. M. Yu, J. Park, and S.-W. Ko, "On-the-fly NLoS detection for wireless positioning: Combinatorial data augmentation approach," in *Proc. IEEE Wireless Commun. Netw. Conf.*, Kuala Lumpur, Malaysia, 2026, to appear.
- [2] H. Chen, H. Sameddeen, T. Ballal, H. Wymeersch, M.-S. Alouini, and T. Y. Al-Naffouri, "A tutorial on terahertz-band localization for 6G communication systems," *IEEE Commun. Surveys Tuts.*, vol. 24, no. 3, pp. 1780–1815, 2022.
- [3] S. Kim, S. Saha, S. Jeong, B. Shim, and M. Z. Win, "Large multimodal model-based environment-aware beam management," *IEEE J. Sel. Areas Commun.*, vol. 44, pp. 991–1007, 2026.
- [4] Y. Etefagh, M. F. Keskin, K. Keykhosravi, G. Seco-Granados, and H. Wymeersch, "Frugal RIS-aided 3D localization with CFO under LoS and NLoS conditions," *IEEE Trans. Veh. Technol.*, pp. 1–14, 2025.
- [5] S. M. Yu, K. Han, J. Park, S.-L. Kim, and S.-W. Ko, "Combinatorial data augmentation: A key enabler to bridge geometry- and data-driven WiFi positioning," *IEEE Trans. Mobile Comput.*, vol. 24, pp. 306–320, 2025.
- [6] I. Guvenc and C.-C. Chong, "A survey on TOA based wireless localization and NLOS mitigation techniques," *IEEE Commun. Surveys Tuts.*, vol. 11, no. 3, pp. 107–124, 2009.
- [7] Y. Yang *et al.*, "Positioning using wireless networks: Applications, recent progress, and future challenges," *IEEE J. Sel. Areas Commun.*, vol. 42, no. 9, pp. 2149–2178, 2024.
- [8] X. Li, E. Leitinger, M. Oskarsson, K. Åström, and F. Tufvesson, "Massive MIMO-based localization and mapping exploiting phase information of multipath components," *IEEE Trans. Wireless Commun.*, vol. 18, no. 9, pp. 4254–4267, 2019.
- [9] A. Fascista *et al.*, "Joint localization, synchronization and mapping via phase-coherent distributed arrays," *IEEE J. Sel. Topics Signal Process.*, vol. 19, no. 2, pp. 412–429, 2025.
- [10] C. Zhou, C. You, C. Zhou, H. Cheng, and S. Shi, "Mixed near-field and far-field localization in extremely large-scale MIMO systems," *arXiv:2503.04681v3*, 2026.
- [11] L. Zhu *et al.*, "A tutorial on movable antennas for wireless networks," *IEEE Commun. Surveys Tuts.*, vol. 28, pp. 3002–3054, 2026.
- [12] H. Xu *et al.*, "Capacity maximization for FAS-assisted multiple access channels," *IEEE Trans. Commun.*, vol. 73, no. 7, pp. 4713–4731, 2025.
- [13] Q. Jiang, X. Shao, and R. Zhang, "Statistical channel-based low-complexity rotation and position optimization for 6D movable antennas enabled wireless communication," *IEEE Trans. Wireless Commun.*, vol. 25, pp. 8874–8889, 2026.
- [14] W. Xia *et al.*, "RIS-empowered integrated location sensing and communication with superimposed pilots," *IEEE Trans. Commun.*, vol. 73, no. 10, pp. 9644–9657, 2025.
- [15] J. Kang, S.-W. Ko, and S. Kim, "Near-field localization with RIS via two-dimensional signal path classification," *IEEE Trans. Wireless Commun.*, vol. 24, no. 4, pp. 3417–3432, 2025.

- [16] Technical Specification Group, “Study on 6G use cases and service requirements; stage 1,” *3rd Generation Partnership Project (3GPP)*, document TR 22.870 V1.1.0, Release 20, Jan. 2026.
- [17] X. Yang, “NLOS mitigation for UWB localization based on sparse pseudo-input Gaussian process,” *IEEE Sensors J.*, vol. 18, no. 10, pp. 4311–4316, 2018.
- [18] Q. Wang, I. Balasingham, M. Zhang, and X. Huang, “Improving RSS-based ranging in LOS-NLOS scenario using GMMs,” *IEEE Commun. Lett.*, vol. 15, no. 10, pp. 1065–1067, 2011.
- [19] S. Marano, W. M. Gifford, H. Wymeersch, and M. Z. Win, “NLOS identification and mitigation for localization based on UWB experimental data,” *IEEE J. Sel. Areas Commun.*, vol. 28, pp. 1026–1035, 2010.
- [20] C. Huang *et al.*, “Machine learning-enabled LOS/NLOS identification for MIMO systems in dynamic environments,” *IEEE Trans. Wireless Commun.*, vol. 19, no. 6, pp. 3643–3657, 2020.
- [21] B. C. Tedeschini, M. Nicoli, and M. Z. Win, “On the latent space of mmWave MIMO channels for NLOS identification in 5G-advanced systems,” *IEEE J. Sel. Areas Commun.*, vol. 41, no. 6, pp. 1655–1669, 2023.
- [22] J.-S. Choi, W.-H. Lee, J.-H. Lee, J.-H. Lee, and S.-C. Kim, “Deep learning based NLOS identification with commodity WLAN devices,” *IEEE Trans. Veh. Technol.*, vol. 67, no. 4, pp. 3295–3303, 2018.
- [23] H. Yang *et al.*, “Fuzzy transformer machine learning for UWB NLOS identification and ranging mitigation,” *IEEE Trans. Instrum. Meas.*, vol. 74, pp. 1–17, 2025.
- [24] G. Torsoli, M. Z. Win, and A. Conti, “Blockage intelligence in complex environments for beyond 5G localization,” *IEEE J. Sel. Areas Commun.*, vol. 41, no. 6, pp. 1688–1701, 2023.
- [25] X. Zhu, W. Qu, T. Qiu, L. Zhao, M. Atiquzzaman, and D. O. Wu, “Indoor intelligent fingerprint-based localization: Principles, approaches and challenges,” *IEEE Commun. Surveys Tuts.*, vol. 22, no. 4, pp. 2634–2657, 2020.
- [26] X. Xu *et al.*, “Swin-loc: Transformer-based CSI fingerprinting indoor localization with MIMO ISAC system,” *IEEE Trans. Veh. Technol.*, vol. 73, no. 8, pp. 11 664–11 679, 2024.
- [27] X. Wang *et al.*, “Resilient 3D indoor localization using a masked Transformer encoder with multi-band CSI fingerprints,” *IEEE Trans. Wireless Commun.*, vol. 25, pp. 4391–4404, 2026.
- [28] N. S. Bhatia, P. Kocheta, R. Elliott, H. S. Kuttivelil, and K. Obraczka, “Indoor localization using compact, telemetry-agnostic, transfer-learning enabled decoder-only Transformer,” *arXiv:2510.11926*, 2025.
- [29] F. Morselli, S. Modarres Razavi, M. Z. Win, and A. Conti, “Soft information-based localization for 5G networks and beyond,” *IEEE Trans. Wireless Commun.*, vol. 22, no. 12, pp. 9923–9938, 2023.
- [30] W. Zhou *et al.*, “Channel scenario extensions, identifications, and adaptive modeling for 6G wireless communications,” *IEEE Internet Things J.*, vol. 11, no. 5, pp. 7285–7308, 2024.
- [31] A. Conti, G. Torsoli, C. A. Gómez-Vega, A. Vaccari, G. Mazzini, and M. Z. Win, “3GPP-compliant datasets for xG location-aware networks,” *IEEE Open J. Veh. Technol.*, vol. 5, pp. 473–484, 2024.
- [32] H. Jung, S.-W. Ko, and S. Kim, “Toward cooperative localization with implicit connectivity: Graph neural network approach,” *IEEE Wireless Commun. Lett.*, vol. 14, no. 10, pp. 3184–3188, 2025.
- [33] Z. Kang, Y. Lim, Z. Gu, S.-W. Ko, T. Q. Quek, and J. Park, “Vision-language-model-guided differentiable ray tracing for fast and accurate multi-material RF parameter estimation,” *arXiv:2601.18242*, 2026.
- [34] C. Mensing and S. Plass, “Positioning algorithms for cellular networks using TDOA,” in *Proc. IEEE Int. Conf. Acoust. Speech Signal Process.*, vol. 4, 2006, pp. 4–4.
- [35] A. Gretton, K. Borgwardt, M. Rasch, B. Schölkopf, and A. Smola, “A kernel method for the two-sample problem,” in *Proc. Adv. Neural Inf. Process. Syst.*, vol. 19, 2006, pp. 513–520.
- [36] Technical Specification Group Radio Access Network, “Study on channel model for frequencies from 0.5 to 100 GHz,” *3rd Generation Partnership Project (3GPP)*, document TR 38.901 V19.2.0, Release 19, Dec. 2025.
- [37] T. Zhang, Y. Wang, M. Ouyang, L. Xing, S. Ma, and F. Gao, “An RFSoc prototype for third-party camera aided mmWave communications,” *IEEE Trans. Commun.*, vol. 73, no. 4, pp. 2769–2785, 2025.